Quantum phase diagram of a frustrated antiferromagnet on the bilayer honeycomb lattice

Hao Zhang, Carlos A. Lamas, Marcelo Arlego, and Wolfram Brenig

Phys. Rev. B **93**, 235150 — Published 27 June 2016

DOI: 10.1103/PhysRevB.93.235150

Quantum phase diagram of a frustrated antiferromagnet on the bilayer honeycomb lattice

Hao Zhang,[1,*] Carlos A. Lamas,[2,†] Marcelo Arlego,[2] and Wolfram Brenig[3,‡]

[1] *Beijing National Laboratory for Condensed Matter Physics and Institute of Physics, Chinese Academy of Sciences, Beijing 100190, China*

[2] *IFLP, UNLP, CONICET, Facultad de Ciencias Exactas, calle 49 y 115, La Plata, Argentina*

[3] *Institute for Theoretical Physics, Technical University Braunschweig, D-38106 Braunschweig, Germany*

We study the spin-1/2 Heisenberg antiferromagnet on a bilayer honeycomb lattice including interlayer frustration. Using a set of complementary approaches, namely Schwinger bosons, dimer series expansion, bond operators, and exact diagonalization, we map out the quantum phase diagram. Analyzing ground state energies and elementary excitation spectra, we find four distinct phases, corresponding to three collinear magnetic long range ordered states, and one quantum disordered interlayer dimer phase. We detail, that the latter phase is adiabatically connected to an *exact* singlet product ground state of the the bilayer which exists along a line of maximum interlayer frustration. The order within the remaining three phases will be clarified.

I. INTRODUCTION

Disordered phases in frustrated two-dimensional spin systems are a very active field of research which thrives both, on the synthesis of new materials as well as the development of new theoretical concepts[1–4]. In this context, Heisenberg antiferromagnets on the honeycomb lattice have attracted considerable interest recently. $Bi_3Mn_4O_{12}(NO_3)$, discovered by Smirnova *et al.*[5] is among the materials to display this structure, with Mn^{4+} ions with $S = 3/2$ forming an undistorted honeycomb lattice. Two honeycomb layers are separated by bismuth atoms, resulting in a bilayer arrangement, thereby introducing the additional ingredient of a bilayer honeycomb magnet.

Ab initio calculations, by Kandpal and van den Brink[6] have suggested that in $Bi_3Mn_4O_{12}(NO_3)$ the interlayer exchanges are the dominant couplings, followed by intralayer nearest neighbor interactions. Compared to the latter two, frustrating intralayer, second and third neighbors couplings have been evaluated, to be approximately one order of magnitude smaller. Particularly important however, (see Fig. 2 A of Ref. 6), the interlayer exchange has been found to be strongly frustrated. Disordered magnetic ground states, which have been observed experimentally[7], have been suggested to result from competing interactions. While theoretically, substantial progress has been made regarding the effects of intralayer frustration and quantum disordered phases in the single-layer honeycomb magnet[8–23], less attention has been given to the the influence of an interlayer coupling in their impact on disordered phases[13,24–26].

The aim of this work is to study the zero temperature phase diagram of a frustrated Heisenberg model on the bilayer honeycomb lattice including interlayer frustration. At a particular value of maximum interlayer frustration we obtain an exactly solvable model, with a dimerised ground state. We focus on the $S = 1/2$ case, where quantum fluctuations become more important, although some results remain valid for larger values of the spin, as we discuss in the following. We explore the quantum phases of the model in the exchange parameter space surrounding the exact dimer state, using various complementary techniques, including bond operators (BO), Schwinger boson mean field theory (SB-MFT) and series expansion (SE) based on the continuous unitary transformation method. These studies will be complemented with exact diagonalization (ED) using Lanczos on finite systems. We provide results for ground state energies, spin gaps, spin correlation functions, the quantum phase diagram, and the nature of the quantum phase transitions.

The outline of the paper is as follows: Sec. II introduces the model and proves that a product of dimers is the exact ground state of the system on a special line of the parameter space. Sec. III sketches several qualitative aspects of the the quantum phase diagram. In Sec. IV we analyze the interlayer dimer phase, departing from the line of the exact dimer state. In Sec. V we characterize the magnetic phases, including Néel-like and collinear states. In Sec. VI we summarize our quantitative findings on the quantum phase diagram. In Sec. VII we briefly discuss some consequences of adding intralayer frustration by next nearest neighbor exchange. Finally in Sec. VIII we present our conclusions and perspectives. Several appendices are added for technical details regarding the methods we use.

II. MODEL AND EXACT GROUND STATE

We study the Heisenberg Hamiltonian on the bilayer honeycomb lattice

$$H = \sum_{\vec{r},\vec{r}',\alpha,\beta} J_{\alpha,\beta}(\vec{r},\vec{r}')\vec{\mathbf{S}}_\alpha(\vec{r})\cdot\vec{\mathbf{S}}_\beta(\vec{r}'), \qquad (1)$$

where $\vec{\mathbf{S}}_\alpha(\vec{r})$ is the spin operator on site α corresponding to the unit cell $\vec{r}$. The index α takes the values

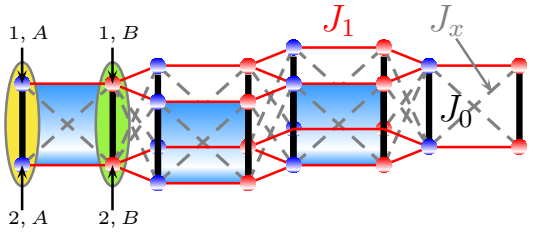

FIG. 1. (Color online) Dominant exchange interactions in $Bi_3Mn_4O_{12}(NO_3)$. Colored areas correspond to the unit cells. Frustrating intralayer next nearest-neighbors interactions are omitted in this figure for simplicity.

$\alpha = 1, A;\ 2, A;\ 1, B;\ 2, B$ corresponding to the four sites on each unit cell and the couplings $J_{\alpha,\beta}(\vec{r},\vec{r}')$ are depicted in Fig. 1. As stated in Sec. I, the inclusion of the frustrating interlayer coupling J_x is motivated by *ab initio* calculations[6]. J_x may be comparable to J_1 and of relevant magnitude with respect to the remaining exchange couplings. In Sec. VII, we also consider intralayer next-nearest neighbors frustrated coupling, which will be labeled J_2, but is not shown in Fig. 1 for simplicity.

In this Section we focus on interlayer frustration only, i.e. $J_2 = 0$. Interestingly, in that case, the bilayer honeycomb belongs to a class of Hamiltonians, which exhibits an exact dimer-product ground state in a certain region of parameter space, even for finite $J_{1,x}$. This result is valid for arbitrary site spin S. Hamiltonians with this property seem to have been constructed first in Ref. 27, based on methods in Ref. 28, and have been reconsidered in many subsequent studies[29–35]. In particular the bilayer square lattice model have been investigated previously[33,34]. However, the relevant point in our work is that we find a bilayer model with the same geometry proposed for the material $Bi_3Mn_4O_{12}(NO_3)$ wich presents an exact dimer product ground state in the region of the parameter space where ab-initio calculations suggest the material may exist.

Using Fig. 2, we start by writing the Hamiltonian Eq. (1) as $H = H_0 + H_1 + H_2$, with

$$H_i = \sum_{\vec{r}} \Big[\frac{J_0}{3} \left(\vec{\mathbf{S}}_{1,A}(\vec{r_i}) \cdot \vec{\mathbf{S}}_{2,A}(\vec{r_i}) + \vec{\mathbf{S}}_{1,B}(\vec{r}) \cdot \vec{\mathbf{S}}_{2,B}(\vec{r}) \right) + J_1 \left(\vec{\mathbf{S}}_{1,A}(\vec{r_i}) \cdot \vec{\mathbf{S}}_{1,B}(\vec{r_i}) + \vec{\mathbf{S}}_{2,A}(\vec{r_i}) \cdot \vec{\mathbf{S}}_{2,B}(\vec{r_i}) \right) + J_x \left(\vec{\mathbf{S}}_{1,A}(\vec{r_i}) \cdot \vec{\mathbf{S}}_{2,B}(\vec{r_i}) + \vec{\mathbf{S}}_{2,A}(\vec{r_i}) \cdot \vec{\mathbf{S}}_{1,B}(\vec{r_i}) \right) \Big], \quad (2)$$

in which $i = 0, 1, 2$ corresponds to $\vec{r}_{(0,1,2)} = \vec{r} + (\vec{0}, \vec{e}_1, \vec{e}_2)$, being $\vec{e}_1$ and $\vec{e}_2$ the primitive vectors of the triangular lattice. Introducing the bond spin operators

$$\vec{\mathbf{L}}_\alpha = \vec{\mathbf{S}}_{1,\alpha} + \vec{\mathbf{S}}_{2,\alpha} \qquad \vec{\mathbf{K}}_\alpha = \vec{\mathbf{S}}_{1,\alpha} - \vec{\mathbf{S}}_{2,\alpha}. \quad (3)$$

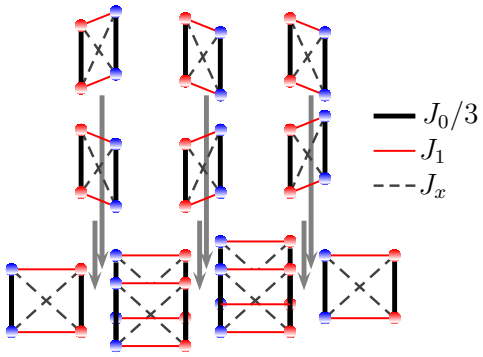

FIG. 2. (Color online) Decomposition of the Heisenberg model on the frustrated bilayer honeycomb lattice into three sets of four-spin plaquets.

with $\alpha = A, B$, we can rewrite H_0 as

$$H_0 = -2J_0 NS(S+1) + \sum_{\vec{r}} \Big\{ \frac{J_0}{2} \left(\vec{\mathbf{L}}_A^2(\vec{r}) + \vec{\mathbf{L}}_B^2(\vec{r}) \right) + \left(\frac{J_1 + J_x}{2} \right) \left(\vec{\mathbf{L}}_A(\vec{r}) \cdot \vec{\mathbf{L}}_B(\vec{r}) \right) + \left(\frac{J_1 - J_x}{2} \right) \left(\vec{\mathbf{K}}_A(\vec{r}) \cdot \vec{\mathbf{K}}_B(\vec{r}) \right) \Big\}, \quad (4)$$

with similar expressions for H_1 and H_2.

The main point of this Section is, that for $J_1 = J_x$, the last term in the Hamiltonian vanishes, and therefore, (i) *each* bond spin $\vec{\mathbf{L}}_A(\vec{r})$ is conserved and (ii) the *total* bond spin $\sum_{\vec{r}} \vec{\mathbf{L}}_A(\vec{r})$ is conserved. Therefore, at $J_1 = J_x$, the eigenstates of H are multiplets of the total bond spin. Among those is the *product state of bond singlets*, i.e. $|\psi\rangle = \bigotimes_{i=1}^{N} |s_A\rangle_{\vec{r}_i} |s_B\rangle_{\vec{r}_i}$ with $\vec{\mathbf{L}}_\alpha(\vec{r}_i)|s_\alpha\rangle_{\vec{r}_i} = 0$, and $|s_\alpha\rangle_{\vec{r}_i} = \sum_{m=-S}^{S} (-1)^{S-m} |m, -m\rangle / \sqrt{2S+1}$. Here $|m, -m\rangle$ labels a product of eigenstates of $\mathbf{S}^z_{1;\alpha}(\vec{r}_i)$ and $\mathbf{S}^z_{2;\alpha}(\vec{r}_i)$ on dimer α of the unit cell located at $\vec{r}_i$. The energy E_0 of $|\psi\rangle$ can be read off from Eq. (4), namely $E_0 = -J_0 NS(S+1)$.

For any other multiplets of the *total* bond spin one has to promote dimers into eigenstates of $\vec{\mathbf{L}}_\alpha(\vec{r})$ different from zero. This will increase any eigenstate's energy proportional to J_0, due to the first term under sum in Eq. (4), but will also lead to exchange-lowering of the energy proportional to $J_1 + J_x$ from pairs of nearest neighbor dimers with non-zero bond spin due to the second term under sum in Eq. (4). Therefore, for any finite site spin S, and for J_1 less than a critical coupling $0 < J_1 < J_1^c$, $|\psi\rangle$ is indeed also the ground state at $J_1 = J_x$.

While we emphasize, that the preceding is valid for *any* site spin S, the nature of the state for $J_1 > J_1^c$ at $J_1 = J_x$ may depend on details. However, for $S = 1/2$ the situation is definite. Since there are only two eigenstates of $\vec{\mathbf{L}}_A(\vec{r})$, i.e. singlet and triplet, the ground state will either be $|\psi\rangle$ or stem from the sector of *all* $\vec{\mathbf{L}}_\alpha(\vec{r})$ in triplet states $|t_{\mu\alpha}\rangle_{\vec{r}_i}$, where μ refers to the z-component. By virtue of Eq. (4) the latter sector is isomorphic to

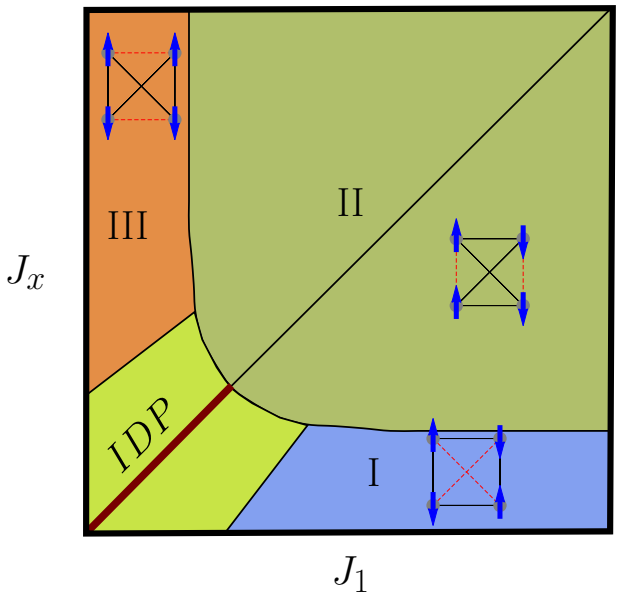

FIG. 3. Qualitative sketch of quantum phase diagram of Heisenberg model on the frustrated bilayer honeycomb lattice

the spin-1 Heisenberg model on the hexagonal lattice. In both of these sector nucleation of inhomogeneous distributions of $L = 0$ and $L = 1$ are energetically unfavorable, i.e. do not lead to ground states.

The exact dimer singlet product state serves as a convenient starting point for several perturbative and mean field methods, which we will take advantage of starting with Sec. IV.

III. QUALITATIVE ASPECTS

In order to pave the way through the remainder of this work, we provide a *qualitative* picture of the quantum phase diagram to be expected for the bilayer without intralayer frustration ($J_2 = 0$) in this Section. This is depicted in Fig. 3. A *quantitative* justification will be given in the following Sections by analyzing various regions of this anticipated phase diagram, considering ground state energies, low energy excitations, triplet gaps, order parameters and spin correlations as extracted from complementary methods, specifically exact diagonalization, Schwinger boson and bond operator mean field theories, series expansion and linear spin-wave theory.

Several comments apply to Fig. 3. First, the diagram is symmetric respect to the $J_1 = J_x$ line. This is evident at the Hamiltonian level. Indeed, from Fig. 1 we see that exchanging $J_1 \leftrightarrow J_x$, induces a site exchange $1, B \leftrightarrow 2, B$, which in turn results in $K_B \leftrightarrow -K_B$. This leaves the last term of H_0 in Eq.(4) invariant. The same is true for H_1 and H_2. In the following we normalize energies in units of J_0 and introduce the dimensionless couplings $j_0 = 1$, $j_1 = J_1/J_0$, $j_2 = J_2/J_0$ and $j_x = J_x/J_0$.

The bold dark-red section of the diagonal line of maximum frustration, $j_1 = j_x$ in Fig. 3, refers to the exact dimer state. As discussed in Sec. II this state terminates in a first order transition point into the ground state of an $S = 1$ AFM Heisenberg on the single layer hexagonal lattice, which extends over the solid black diagonal line shown in Fig. 3. We will show, that this occurs at $j_1 = j_x \simeq 0.5$.

Departing off the line of maximum frustration the exact dimer turns into a gaped *interlayer dimer phase* (IDP) (see Fig. 3). This phase is quantum disordered, and shows dispersive triplon excitations. The triplon gap will decrease from $\Delta = 1$ as distance increases from the diagonal line.

For sufficiently large j_1 and/or j_x, the system will favor collinear order with a straightforward semi-classical interpretation. Namely three possibilities exist to minimize two out of the three exchange energies, leaving one of them frustrated. The corresponding spin arrangements and phases are labeled I, II, and III in Fig. 3, with the frustrated link marked by red dashes. Phases I and III obey the $j_1 \leftrightarrow j_x$ symmetry already mentioned. While the classical states I, II and III do not represent exact eigenstates of the Hamiltonian, we detect signals of these orderings in the quantum model, which justify this identification.

We end this Section by expressing some expectations, regarding the order of the phase transitions. Since the symmetry of phases I, II, and III have no subgroup relations, we expect the transitions I-II and II-III to be of first order, i.e. of level-crossing type. On the other hand, the transition from the IDP into the magnetic phases I and III will be signaled by the closure of the IDP spin gap Δ, which decreases symmetrically from 1 to 0, off the red exact-dimer product line up to the two corresponding critical lines. This gap closure signals a second order quantum phase transition.

Finally, as discussed in Sec. II, the transition from the tip of the bold dark-red line in the IDP to phase II is first order. The nature of the transition remains first order all along the IDP-II transition up to the two tricritical points, separating IDP-I-II and IDP-II-III phases.

IV. INTERLAYER DIMER PHASE

In this Section we analyze the interlayer dimer phase (IDP) at $j_1, j_x \ll 1$. In particular, we discuss our results for the ground state energy and the spin gap, as obtained from dimer series expansion (D-SE), bond operator (BO) theory using Holstein-Primakoff (HP) and mean-field theory (MFT), as well as from exact diagonalization (ED). Both, D-SE and BO-HP/MFT are natural approaches to treat the IDP, since they are both exact in the fully decoupled dimer-product state, along the line $j_1 = j_x$ and treat deviations from the latter perturbatively. While D-SE is exact order-by-order in $j_1 - j_x$, BO-HP/MFT is perturbatively proper only to leading

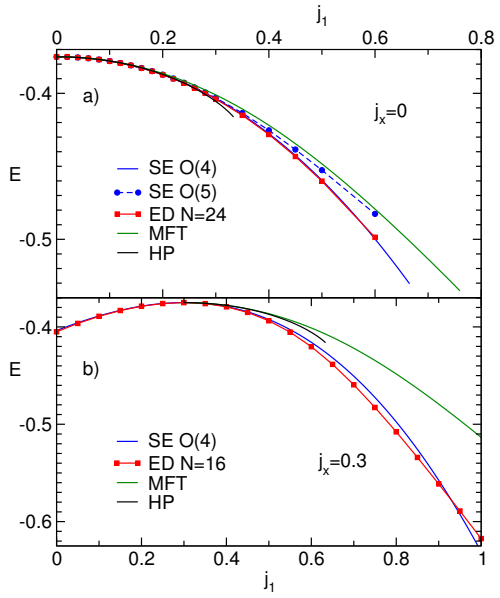

FIG. 4. (Color online) Ground state energy per spin E at $j_2 = 0$ versus j_1 from ED (red with squares), D-SE (blue, blue dashed with circles), BO-HP (black) and BO-MFT (green) for a) $j_x = 0$ with system size $N = 24$, and orders $O(4)$ and $O(5)$, see also Refs. 26, 36, and 37 and b) $j_x = 0.3$ with system size $N = 24$, and order $O(4)$.

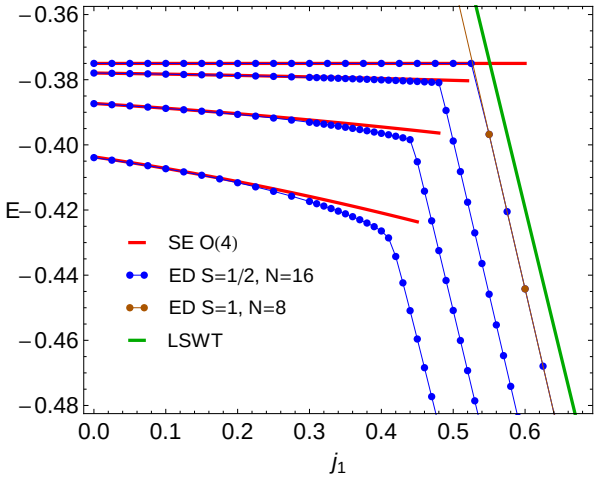

FIG. 5. (Color online) Ground state energy per spin E vs j_1, for different paths parametrized by $b = j_x - j_1$, with $b =$ 0, 0.1, 0.2, and 0.3 (top to bottom). Line-connected blue (brown) dots: ED for S=1/2 (S=1) bilayer (effective single layer). Solid red: D-SE. Green: LSWT for S=1 effective single layer.

order. Since both approaches renormalize only the fully decoupled dimer-product state, they are insensitive to level crossing, which may occur within the ground state, as a function of $j_1 - j_x$. In turn, these methods do not detect first order, but only second order quantum phase transitions accompanied by the closure of a spin gap. Therefore, in order to probe for first order transitions, we resort to ED as an unbiased technique. While finite size effects, render ED less effective to detect gap closures, it allows to search for level crossings rather effectively. In turn ED, BO, and D-SE are complementary to determine the extent of IDP phase, as well as the nature of the transitions also to the other phases present in the model. Technical details about the implementation of the different methods can be found in the Appendices.

We begin by considering the ground state energy. From D-SE we obtain the following O(4) expression for the ground state energy *per spin* evolving from the limit of decoupled interlayer dimers

$$E(j_1, j_x) = -\frac{3}{8} + \frac{9}{512}(j_1 - j_x)^2 \Big[-16 - 8(j_1 + j_x) + 3\left(j_1^2 + j_x^2\right) - 22 j_1 j_x \Big]. \quad (5)$$

This explicitly satisfies $E(j_1, j_1) = -\frac{3}{8}$, corresponding the exact dimer-product solution along $j_x = j_1$ and $E(j_1, j_x) = E(j_x, j_1)$ fulfilling the Hamiltonian invariance under $j_1 \leftrightarrow j_x$. In Fig. 4 we compare the ground state energy obtained from the various methods for two different values of j_x. Fig. 4a), in part also contains BO-MFT solutions from Refs. 36 and 37 and results from Ref. 26, where $O(5)$ D-SE is available at $j_x = 0$, and ED for $N = 24$ sites. In both panels and for all methods, the energy shows a maximum at $j_1 = j_x$, where the ground state is a dimer-product state with energy per spin equal to $-3/8$. Around the exact solution point, ED and D-SE show excellent agreement up to $|j_1 - j_x| \simeq 0.2 \ldots 0.3$ in both panels. Deviations between ED and D-SE beyond that points are due to finite size effects of the ED and due the finite order of the D-SE. The impact of the latter can be assessed at $j_x = 0$, where higher orders of the D-SE have been reached[26]. From Fig. 4a), clearly visible differences arise between $O(4)$ and $O(5)$ D-SE for $|j_1 - j_x| \gtrsim 0.3$. Turning to the BO theory, two comments are in order. First, the HP spin gap closes within the range of j_1, j_x-values depicted. Therefore, the BO curves terminate. Second, both HP and MFT depend on j_1 and j_x only via the difference $j_1 - j_x$. This is not an exact property of the model beyond leading order, which is obvious e.g. from Eq. (5). In turn, BO results are identical for Fig. 4a) and b) up to a shift of origin and have been plotted only for positive $j_1 - j_x$. Moreover, agreement between ED, D-SE and BO is expected to be best at either $j_1 = 0$ or $j_x = 0$, which is consistent with this figure. In fact, the agreement between all four methods is excellent for $j_x = 0$ and for $j_1 \lesssim 0.3$, while ED and D-SE show some difference to BO theory at $j_x = 0.3$. In view of the significant changes from $O(4)$ to $O(5)$ D-SE, a quantitative assessment of these differences is beyond this work. In fact, Fig. 4a) would suggest that $O(5)$ D-SE agrees better with BO theory than with ED for $j_1 \gtrsim 0.3$.

While the variations of results between the methods discussed so far are quantitative only, we expect a qualitative difference between ED and D-SE or BO theory in

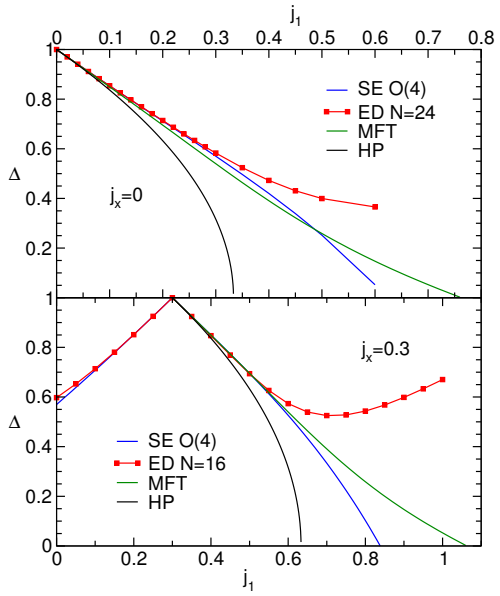

FIG. 6. (Color online) Spin gap Δ versus j_1 from ED (red with squares), $O(4)$ D-SE (blue), BO-HP (black), and BO-MFT (green), for a) at $j_x = 0$ with system size $N = 24$, see also refs.[26,36,37] and b) $j_x = 0.3$ with system size $N = 24$.

the vicinity of the first order transition from the IDP to the magnetic phase II (Fig. 3). Therefore, in Fig. 5 we depict the ground state energy per spin versus j_x along lines parametrized by $b = j_x - j_1$, with $b = 0$, 0.1, 0.2, and 0.3 from top to bottom. ED results are shown by line-connected blue dots, whereas D-SE results are shown by solid red lines. First, the small, albeit finite slope of E at small j_1 in this figure, which is increasing as b increases, demonstrates once more, that properties of the system in the IDP are not only functions of $b = j_x - j_1$. Therefore, in this figure we do not consider BO results. Second, we note that for $b = 0$ ($j_1 = j_x$) the upper pair of curves representing ED and D-SE coincide exactly at $-3/8$ up to a critical point of $j_1^c, j_x^c \simeq 0.52$. This corresponds to the bold red line in Fig. 3. At the critical point, ED exhibits a kink in the energy versus j_1, signaling a first order transition into another type of ground state of the system. Clearly D-SE cannot detect this transition because it adiabatically evolves the dimer state with j_1, which discontinues to be the ground state for $j_1 > j_c^c$. Qualitative differences between ED and D-SE are also observed off the diagonal line, for j_1 roughly larger than j_1^c. Here again, a clear change of slope is detected by ED in Fig. 5 for $b = 0.1, 0.2$. This supports our claim that the transition IDP-II is first order, as anticipated in the previous Section. At $b = 0.3$, ED shows no clear signature of a single kink anymore, suggesting a succession of second and then first-order transitions, close to one of the tricritical points of Fig. 3.

Non-IDP phases will be analyzed in detail in the following Sections. Here we elaborate further on the transition from the IDP into the effective $S = 1$ AFM on the single layer hexagonal lattice anticipated already in Sec. II. We have verified this scenario using two checks. First, we have performed ED calculations on a *single* layer spin-1 cluster comprising the same *site*-geometry as that of the *dimers* in the original cluster. The corresponding ground state energy is depicted by line-connected brown dots in Fig. 5. The excellent agreement between both types of ED calculations verifies our assertion. For a second check, we have considered linear spin wave theory (LSWT) for the ground state energy of the spin-1 Heisenberg antiferromagnet on the hexagonal lattice. For details see appendix D. The result, also shown in Fig. 5, is quantitatively very similar to the ED results, with $j_1^c \simeq 0.551$. Since LSWT for a collinear state with $S = 1$ should be rather well defined, it would be interesting to analyze if the small difference of the critical coupling $\Delta j_1^c \approx 0.03$ between ED and LSWT is dominated by $O(1/S^2)$ correction or by finite size effects.

Perpendicular to the exact dimer line, the dispersion of triplons will lead to a closure of the spin gap Δ at $k_c = (0, 0)$ for sufficiently large $j_1 - j_x$. From $O(4)$ D-SE we get

$$\Delta(j_1, j_x) = 1 - \frac{3}{16}\,|j_1 - j_x| \left| -8 + (j_1 - j_x)^2\,(j_1 - j_x) \right| - \frac{3}{128}\,(j_1 - j_x)^2 \Big[-16 + 8(j_1 - j_x) + 55\,(j_1^2 + j_x) - 14 j_1 j_x \Big]. \quad (6)$$

As for the ground state energy, Eq. (5), this satisfies $\Delta(j_1, j_x) = \Delta(j_x, j_1)$ and resembles the decoupled dimer state, i.e. $\Delta(j_1, j_1) = 1$. In Fig. 6 we compare Eq. (6) with ED, BO-HP and BO-MFT versus j_1 for the same two values of j_x as in Fig. 4. As for the ground state energy, the BO results are identical for Fig. 6a) and b) up to a shift of origin and have been plotted only for positive $j_1 - j_x$. As is clear from the figure, ED, D-SE, and BO-MFT tend to keep the spin gap open for a larger range of exchange couplings off the exact dimer state, while the BO-HP gap closes more rapidly. The agreement between ED, D-SE, and BO-MFT is very good for $|j_1 - j_x| \lesssim 0.3$. It is obvious, that finite size effects for the spin gap in the ED are rather large, showing a minimum of Δ of ~ 0.35 at $N = 24$, versus ~ 0.5 only for $N = 24$. A proper finite-size scaling analysis of the spin gap from ED is unfeasible, because of the large unit cell. Interestingly, while BO-HP shows standard square root behavior of the gap at the critical point, with a negative curvature, self-consistency within the BO-MFT leads to a positive curvature of Δ, with no obvious power law at gap closure.

We close this Section with two remarks on SB-MFT. Also in this approach, quantum disordered phases are associated with a gapped excitation spectrum. In turn, the IDP can equally well be detected using SB-MFT. However, while in the D-SE and BO theory the elementary excitations in the IDP actually correspond to the physical triplons, in SB-MFT they are fractionalized bosonic spinons. The latter are unphysical in the IDP. In order to obtain a proper spin spectrum and the gap, the

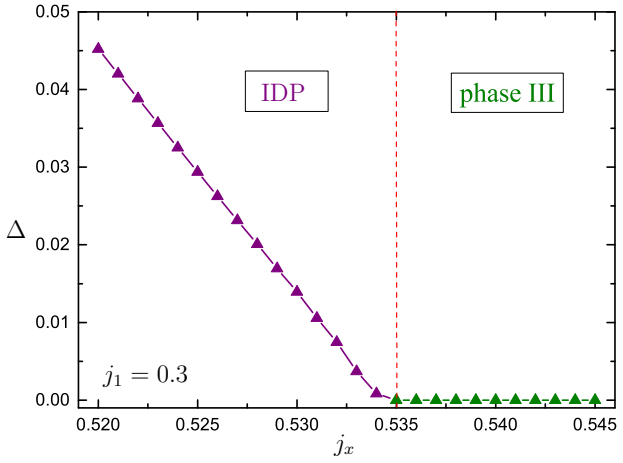

FIG. 7. (Color online) Example of SB-MFT gap along vertical cut through the phase diagram Fig. 3, at $j_1 = 0.3$ for the IDP-III transition and extrapolated to the thermodynamic limit.

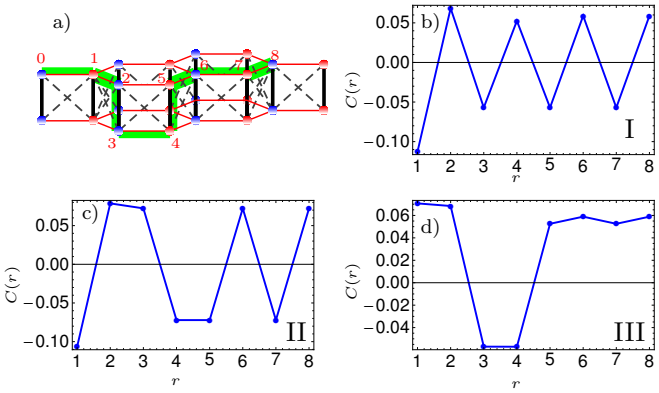

FIG. 8. (Color online) Static correlation function $C(r)$ vs. r along the green path depicted in panel a), obtained by means of ED on a finite cluster of 24 spins. Panel b) $j_{1,x} = 0.7, 0.3$, c) $j_{1,x} = 0.7, 0.7$, and d) $j_{1,x} = 0.3, 0.7$ clearly show a pattern consistent with the classical structure shown in regions I, II, and III of Fig. 3.

two-spinon propagator would have to be evaluated, see e.g. Ref. 38, however *including* interactions beyond Ref. 38, in order to confine the spinon into a sharp triplon mode. We will not perform such calculations. Despite of this, it is perfectly valid to use SB-MFT to extract transition points from the IDP into the magnetic phases of the bilayer from a closure of the spinon gap, since long range magnetic order is characterized by a condensation of the bosons at some wave vector leading to a gapless spectrum. In Fig. 7 we show a representative example. As the second remark, let us note that SB-MFT predicts a critical point $j_1^c = 0.547$ on the $j_1 = j_x$ line for the transition IDP-II, which agrees very well with the LSWT prediction given by $j_1^c = 0.551$, and therefore is larger than ED, similar to the latter.

V. MAGNETIC PHASES

In this Section we analyze quantum properties of the phases I, II and III of Fig. 3. These are gapless states with magnetic long-range order (LRO) and a spin structure, which has been explained on the classical level in Sec. III.

To investigate how the signatures of these orderings survive under quantum fluctuations, we evaluate the static correlation functions $C(r) = \langle S_0^z S_r^z \rangle$. In panels (b-d) of Fig. 8 we show $C(r)$ vs r along the green path depicted in panel (a), calculated by means of ED on a finite cluster of 24 spins. We have selected three different points of parameters space to illustrate the behavior of the correlations along the considered path. In panel (b) we show $C(r)$ for the point $(j_1 = 0.7, j_x = 0.3)$, whereas in panel (d) we depict the correlation for the symmetric point $(j_x = 0.7, j_1 = 0.3)$. As it can be observed, in both cases the sign alternation in $C(r)$ is consistent with the magnetically ordered phases I and III illustrated in the insets of Fig. 3. The same occurs with panel (c), which shows $C(r)$'s dependence on r for $(j_x = 0.7, j_1 = 0.7)$. In this case the behavior of the correlation is consistent with the classical spin pattern depicted in the inset of phase II in Fig. 3.

Although we can verify short-distance correlations consistent with the ordered phases by means of ED, the finite cluster size imposes severe constraints and does, for example, not permit to consider the actual form of $C(r)$ and to claim LRO in the sense of $C(r \to \infty) = const.$

These aspects can be considered with complementary techniques, such as Schwinger bosons mean field theory (SB-MFT). This approach has been successfully used to study two-dimensional frustrated Heisenberg antiferromagnets[12,21,26,39,40]. We refer to Appendix B for details about this technique.

Fig. 9 shows the spin-spin correlation calculated by means SB-MFT between spins belonging to the same layer, and traversing the layer along one of the 'zigzag-chain' paths of the hexagonal lattice, for a system of 10000 sites at $j_1 = 0.8$, $j_x = 0.3$ (phase I); $j_1 = 0.9$, $j_x = 0.6$ (phase II); and $j_1 = 0.52$, $j_x = 0.3$ (IDP). The last case is depicted for a contrast to the magnetic phases. Due to the mirror symmetry of the phase diagram along the line $j_1 = j_x$, we confine the figure to $j_1 \geqslant j_x$. While AFM LRO is clearly visible in panels (a) and (b) on each layer, the difference between (a) and (b) is with the nearest-neighbor interlayer correlation (not depicted). We find the latter to be AFM in phase I and FM in phase II, in agreement with the Lanczos results. Panel (c) of Fig. 9 clearly shows, that the IDP phase only has short range spin-spin correlations, consistently with a finite gap.

To determine the location of the transitions between the LRO phases we may use, that these phases have no subgroup relations, and therefore any direct transitions between them is of first order, i.e. they can be determined from a discontinuity in the ground state energy. This is

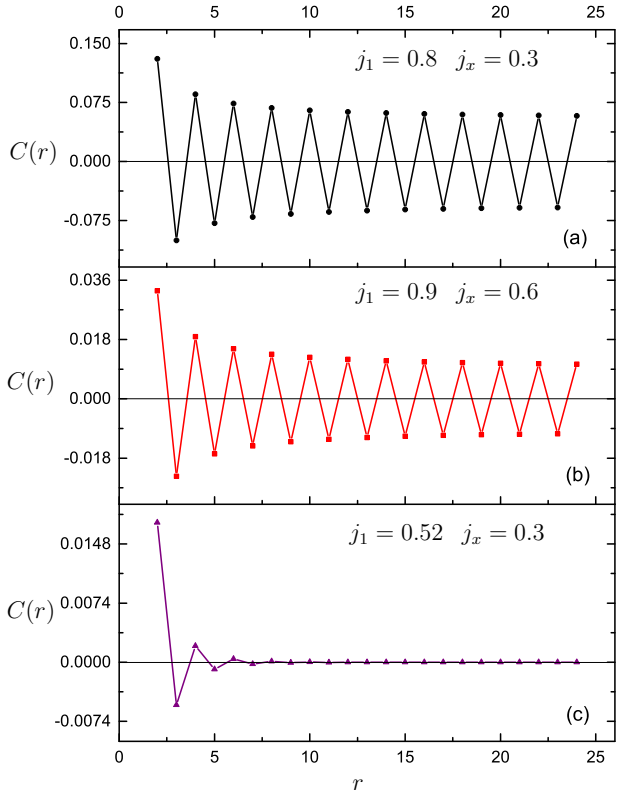

FIG. 9. (Color online) Spin-spin correlation between spins belonging to the same layer in the zigzag direction obtained by SBMFT for a 10000 sites system. It is shown for the three different phases in the $j_1 > j_x$ side of the phase diagram (Fig. 3): (a) $j_1 = 0.8$, $j_x = 0.3$ (phase I), (b) $j_1 = 0.9$, $j_x = 0.6$ (phase II), and (c) $j_1 = 0.52$, $j_x = 0.3$ (IDP).

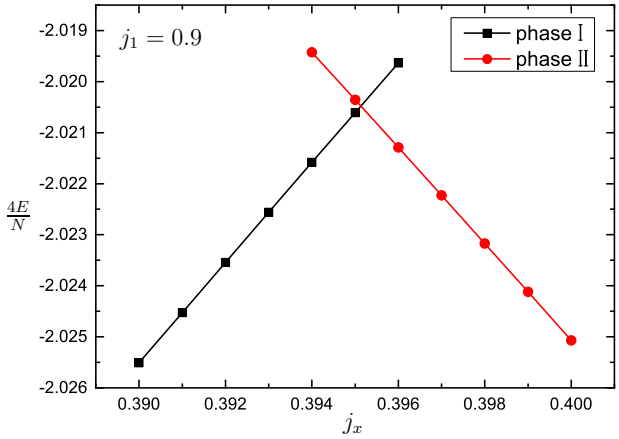

FIG. 10. (Color online) Energy per unit cell from SB-MFT along a vertical cut through the phase diagram (Fig. 3) at $j_1 = 0.9$ for the phase transition I-II.

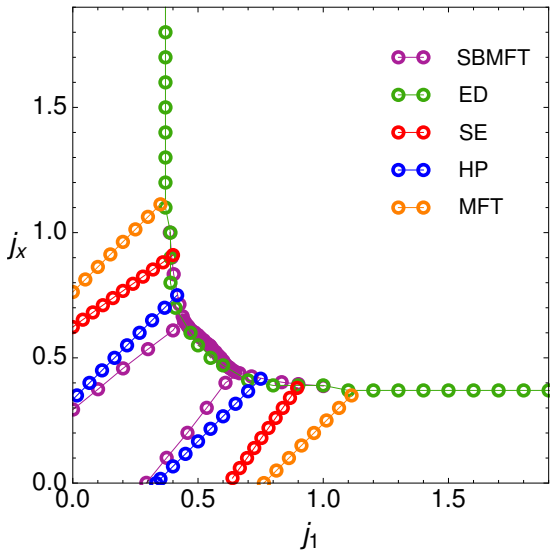

FIG. 11. Quantum phases and critical lines determined by the different techniques considered.

true, both, for ED and SB-MFT. In Fig. 10 a representative example obtained from the latter is depicted for a vertical cut through Fig. 3. Similar results are obtained from ED and will be summarized in the next Section.

Let us finally mention that we have not obtained any evidence of the existence of intermediate phases (e.g. exhibiting non-collinear structures like helical order) between I-II or II-III phases. However, the limitations of the techniques employed, especially the reduced sizes which ED achieves, as well as the mean field character of SB-MFT, does not allow completely discard the existence of such phases.

VI. QUANTUM PHASE DIAGRAM

In this Section we compare the critical lines for the phase transitions of the system obtained from all complementary methods of this work. As a central result Fig. 11 compiles our findings from SB-MFT, BO-HP, BO-MFT, D-SE, and ED. This figure is the *quantitative* analog of the *qualitative* sketch in Fig. 3. Several comments are in order.

To begin, we note that for the first order transitions, i.e. I↔II, II↔III, and IDP↔II, there is a very good quantitative agreement between SB-MFT and ED, showed by line-connected magenta and green open circles, respectively in Fig. 11. This is expected, since first order transitions are determined by ground state energies. These are less susceptible to errors of different approaches as e.g. finite size effects or mean-field approximations. We note that SB-MFT technique is the only method employed in our work, which potentially allows for an estimation of all critical lines, independently of the character of the transition, i.e. first or second order.

In contrast to the first order transitions, for the second order IDP↔(I, III) transitions, the critical lines obtained from our complementary methods will determine a range of potential transition points at most, since the gap closure, i.e. the behavior of the critical correlation length is sensitive to the method used. Nevertheless it is

clearly visible from Fig. 11, that the symmetric regions of both IDP↔(I, III) transitions are centered around the lines $j_x \sim j_1 \pm 0.6(\pm 0.2)$, where ± 0.2 denotes an uncertainty set by the scatter between the various approaches. Note that this scatter also implies an uncertainty of the location of the two tricritical points separating phases IDP-I-II and IDP-II-III.

Remarkably all techniques predict essentially straight critical lines for the IDP↔(I, III) transitions with approximately unit slope, at least on the scale of the plot. This is a direct consequence of the last term in Eq. 4, perturbing the exact dimer state. As a consequence, e.g. in both BO methods, and by construction, the triplon hopping amplitude is a function of the combination of exchanges $|j_1 - j_x|$ only. Yet, D-SE at $O(4)$ (red open circles in Fig. 11) leads to a small curvature of the transition lines. In BO-HP it is possible to obtain an analytical expression, namely $j_x = j_1 \pm 1/3$, for critical lines (see appendix A), depicted by blue open circles in Fig. 11. For BO-MFT (orange open circles in Fig. 11), the offset $1/3$ is replaced through numerical solution of the analytic self-consistency equations by ≈ 0.76 (see Fig. 6a))

Note that in all the cases (except SB-MFT) the second order critical line ends at the border of phase II, which is obviously an artifact of the methods since, as we have previously mentioned, level crossings are not detected by D-SE nor BO techniques.

VII. INTRALAYER FRUSTRATION

In this Section we analyze the effect of frustrating intra-layer J_2 coupling on the model. The results are discussed in a way to make contact with previous analysis of the Heisenberg model on the frustrated bilayer[26] as well as the single layer honeycomb lattice[8,14,19–21,23].

To this end in Fig. 12 we present the phase diagram in the plane $J_2/J_1 - J_0/J_1$, at $J_x = 0$, which enables to incorporate the single layer ($J_0/J_1 = 0$) as a limiting case. Before considering our results, let us briefly comment on some aspects previously investigated. Regarding the frustrated single layer model (along x-axis of Fig. 12), Néel order is present for $J_2/J_1 \lesssim 0.2$. For $0.2 \lesssim J_2/J_1 \lesssim 0.4$ several non-magnetic phases have been proposed to exist, including gapped spin liquids (GSL) and VBC plaquette and dimer phases. However, their extension and the type of phase transitions is still under debate[8,14,19–21,23]. Finally, for larger values of frustration spiral order emerges, which (as the Néel phase) is reminiscent of the classical version of the model.

The Néel phase persists for finite values J_0 and J_2, as illustrated by the gray shaded region in Fig. 12. The blue solid line in this figure refers to the SB-MFT critical line, determined in ref.[26], where, as it can be observed, a re-entrant pocket at small J_0/J_1 was predicted.

In order to relate the latter findings with those of the previous sections, one has to note that the numerical location of critical points depicted along y-axis (J_0/J_1) in

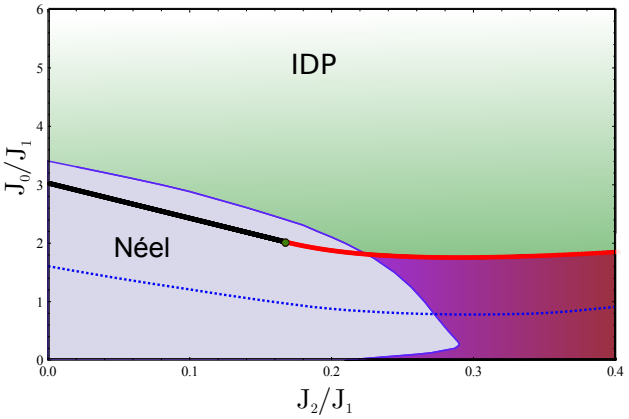

FIG. 12. Numerical Results in the plane $J_2/J_1 - J_0/J_1$. The gray shaded region corresponds to BO-MFT prediction of Néel order. Blue solid line corresponds to SB-MFT critical line determined in ref.[26]. Black and red lines correspond to BO-HP results. Black line-segment correspond to BO-HP results where the critical wave vector is $k_c = (0, 0)$ whereas the red line corresponds to different k_c values. Blue dots corresponds to D-SE results for the transition.

Fig. 12 are inversely related to those shown on x-axis of Fig. 11 (J_1/J_0). Therefore along y-axis of Fig. 12 there is direct second order transition between the IDP, i.e. the green shaded area in the Figure, to the Néel phase, which therefore has to be associated with phase I in the context of the previous sections. This transition is signaled by the closure of the triplet IDP gap.

Next we discuss the evolution of the second order transition into the IDP phase for finite J_2 by analyzing the closure of triplet gap obtained from BO-HP and D-SE techniques. The technical aspects of this analysis are layed out in full detail in appendices A and C. Several comments are in order. First we focus on BO-HP versus SB-MFT. The corresponding quantum critical line from the BO-HP can be dissected into a black line-segment, which terminates at the green point at $(J_2/J_1, J_0/J_1) = (1/6, 2)$, and a red line-segment. On the black line-segment the critical wave vector is $k_c = (0, 0)$. This is consistent with a transition from the IDP phase into the Néel state, which is also obtained from the SB-MFT approach below the blue critical line. It is remarkable, that with only a parallel shift by $\sim 10\%$ the critical lines from SB-MFT and BO-HP can be brought to essentially coincide, from $J_2 = 0$ up to the green point. Beyond the latter, the critical wave vector k_c of the BO-HP starts to be inconsistent with a transition into a Néel state and, accordingly, the critical lines from BO-HP and SB-MFT separate.

As J_2/J_1 increases at fixed J_0/J_1, the interlayer exchange gets less relevant, rendering the IDP phase unfavorable and resulting in an upward curvature of the IDP critical line in this region. In particular, nowhere the BO-HP does stays gapped down to $J_0/J_1 = 0$. Outside of the Néel and IDP phase this implies a region of un-

known phases of the bilayer, i.e. the violet region in Fig. 12. Since exactly *on* the line J_2/J_1 at $J_0/J_1 = 0$ various GSL and VBC phases have been proposed[8,14,19–21,23], it is very tempting to speculate, that such phases are stable to a certain extent against finite interlayer exchange J_0/J_1. This may open the possibility of direct transitions of such phases into the IDP phase. Additionally, the violet region could also host states nonexistent on the line $J_0/J_1 = 0$. The study of such transitions or states is not the purpose of this paper and remains as open issue.

Regarding the transitions along the red BO-HP line, the critical wave vector evolves from that for a Néel state on the black line segment into that of the 120°-order of the triangular lattice antiferromagnet for $J_2/J_1 \gg 1$ - as to be expected, but not visible on the scale of Fig. 12. Interestingly, this evolution is accompanied by the appearance of *line* degeneracies of the triplon dispersion at intermediate and large J_2/J_1. From a technical point of view such degeneracies limit the applicability of the BO-MFT treatment on the *quadratic* level. In fact, power counting for Eq. (A13) shows that the integral on the right hand side diverges for such cases. In turn the MFT gap stays *finite* for all J_2/J_1 displaying line *minima* of the dispersion. This is certainly an artifact, rendering the BO-MFT at quadratic level insufficient for finite J_2/J_1.

Several routes beyond the purely quadratic level of Eqs. (A4)-(A7) exist for BO theory, potentially lifting degeneracies in the dispersion at finite J_2/J_1. However these routes lead to additional issues, which we will not touch upon in the present work. Incorporating triplon interactions either pertubatively, or at the self-consistent Hartree-Fock level[41] is one option. Such approaches however do not *systematically* improve the quadratic low-triplon density approximation and remain uncontrolled. Treating the hard-core constraint Eq. (A2) via infinite on-site triplon repulsion in a T-matrix approximation[42] is another scheme, which however is limited to small triplon density and, while providing excellent results on unfrustrated lattices, has been found to be unsuited for frustrated lattices[41]. Finally, a truly systematic $1/d$-expansion has been proposed very recently[43,44]. Its relevance for $d = 2$ needs further studies.

To close this section, D-SE results are shown with blue dots in Fig. 12. As it can be observed, for small J_2/J_1 D-SE displays the same tendency as SB-MFT and BO-HP, which is similar to the conclusions drawn in the j_1-j_x plane in Fig.11. Note that, at least for $J_2 = 0$, the location of the gap closure, as predicted by D-SE quantitatively is in better agreement with precise QMC determination of this transition at $J_0/J_1 \approx 1.645$[24] than SB-MFT and BO-HP. In that sense SB-MFT and BO-HP overestimate the extent of the Néel phase. In contrast to the BO-HP, the spin gap in $O(4)$ D-SE closes at the single point $k_c = (0, 0)$ in the range depicted in Fig.12. For larger J_2/J_1 deviations with respect to other techniques are occur and also other k_c emerge from D-SE. It would be necessary to go to higher orders within the series, to clarify the k-dependence of gap closure in that regime

VIII. CONCLUSIONS

We have studied the zero temperature quantum phase diagram of the frustrated antiferromagnet on the bilayer honeycomb lattice. To characterize the different phases present in the model, as well as their transitions, we have calculated a variety of quantities, such as ground state energies, low energy excitations, triplet gaps and static spin-spin correlations. This has been done, using several complementary techniques: bond operator and Schwinger bosons mean field theories, dimer series expansion and exact diagonalization of finite systems.

The main results of our work are contained in the schematic phase diagram of Fig. 3. This diagram is symmetric with respect to $j_1 = j_x$. For $j_1 = j_x \leq j_x^c \approx 0.55$ the model exhibits an exact interlayer dimer-product state, whose ground state and elementary triplet excitations are identical to the decoupled dimer limit ($j_1 = j_x = 0$). Perpendicularly to the diagonal line a dimerised phase evolves adiabatically from the exact ground state and extends over a region around the diagonal line. This gapped *interlayer dimer phase* (IDP) has been analyzed by means of bond operator theory and dimer series expansion (complemented with Lanczos diagonalization) since both methods are exact for the singlet product state.

In contrast to the IDP phase, which is a gapped, magnetically disordered, and of quantum origin, the other phases present in the model are gapless, magnetically ordered, and quasi classical. In particular we have determined three magnetic phases, denoted by I, II, and III in Fig. 3. The phases I and II are Néel-like, whereas III exhibits columnar order. The magnetic structure of these phases has been clarified both, by exact diagonalization on finite systems of N=24 sites and by Schwinger bosons mean field theory on large lattices of N=10000 sites, both with identical results. In particular phase II along the diagonal line, for $j_1 = j_x > j_x^c$ is equivalent to the ground state of an effective spin-1 Heisenberg model on the single-layer honeycomb lattice, with an antiferromagnetic coupling $j_1 = j_x$.

All the numerical techniques suggest that the nature of the phase transitions are first order (level crossing) for the transitions I↔II, II↔III and IDP↔II, and second order (gap closure) for the transitions IDP↔I and IDP↔III. A quantitative analysis of the quantum phase diagram, obtained from the combination of all methods has been presented. For all first order transitions good agreement between Lanczos and Schwinger bosons MFT has been obtained. For the second order transitions, qualitative agreement between the different methods used has been shown.

Finally we have briefly explored the effects of intralayer frustration. We find, that both, the IDP and the LRO phase I naturally extend into the j_1-j_2 plane, and are terminated by sufficiently large intralayer frustration j_2.

ACKNOWLEDGMENTS

H.Z. thanks Lu Yu for fruitful discussions, and the Institute of Physics, Chinese Academy of Sciences for financial support. C.A.L. and M.A. are supported by CONICET and FONCyT (PICT 2013-0009). Work of W.B. has been supported in part by the Deutsche Forschungsgemeinschaft through SFB 1143 and by the National Science Foundation under Grant No. NSF PHY11-25915. W.B. also acknowledges kind hospitality of the Platform for Superconductivity and Magnetism, Dresden.

Appendix A: Bond Operator Approach

Quantum spin models comprising weakly coupled antiferromagnetic spin-1/2 dimers allow for a description in terms of bosonic operators, so called *bond operators* (BO)[45–47], which label the dimer's singlet-triplet spectrum. BOs lead to a treatment of dimerised phases similar to the linear spin wave theory for magnetically ordered phases. Within BO theory the two spins $\vec{S}_{i=1,2}$ on each dimer are expressed as

$$S^{\alpha}_{\frac{1}{2}} = \frac{1}{2}(\pm s^{\dagger}t_{\alpha} \pm t^{\dagger}s - \sum_{\beta,\gamma} i\varepsilon_{\alpha\beta\gamma}t^{\dagger}_{\beta}t_{\gamma})\,, \tag{A1}$$

where $s^{(\dagger)}$and $t^{(\dagger)}_{\alpha}$ destroy(create) the singlet and triplet states of the dimer and Greek labels, $\alpha = 1, 2, 3$, refer to the threefold triplet multiplet. A hard-core constraint

$$s^{\dagger}s + \sum_{\alpha} t^{\dagger}_{\alpha}t_{\alpha} = 1 \tag{A2}$$

is implied, which renders the algebra of the r.h.s of Eq. (A1) identical to that of spins.

Inserting the BO representation into a spin model leads to an interacting Bose gas. Two kinds of *quadratic approximations* have become popular in the limit of weak dimer coupling, namely the BO mean-field theory (BO-MFT)[47] and the BO Holstein-Primakoff (BO-HP) approach[45,46]. In both cases, terms only up to second order in the BOs are retained. In the BO-MFT, singlets are condensed by $s^{(\dagger)} \to s \in \mathrm{Re}$ and the constraint Eq. (A2) is satisfied on the average with a global Lagrange multiplier η[47]. In the BO-HP, the constraint is used to eliminate all singlet operators using $s = s^{\dagger} = (1 - \sum_{\alpha} t^{\dagger}_{\alpha}t_{\alpha})^{-1/2}$, followed by expanding the square root[45,46].

For both approaches, i.e. BO-MFT and BO-HP, the Hamiltonian in units of J_0 of our frustrated hexagonal bilayer lattice reads

$$H = H_0 + H_1 + H_2 + H_c \tag{A3}$$

$$H_0 = \sum_{l,b}(-\frac{3}{4}s^2 + \frac{1}{2}\sum_{\alpha} t^{\dagger}_{lb\alpha}t_{lb\alpha}) \tag{A4}$$

$$H_1 = \sum_{l,\widetilde{m},\alpha} \frac{s^2\widetilde{j_1}}{2}(t^{\dagger}_{\widetilde{m}A\alpha}t_{lB\alpha} + t^{\dagger}_{\widetilde{m}A\alpha}t^{\dagger}_{lB\alpha} + h.c.) \tag{A5}$$

$$H_2 = \sum_{l,\widetilde{l},\alpha,b} \frac{s^2 j_2}{2}(t^{\dagger}_{\widetilde{l}b\alpha}t_{lb\alpha} + t^{\dagger}_{\widetilde{l}b\alpha}t^{\dagger}_{lb\alpha} + h.c.) \tag{A6}$$

$$H_c = -\sum_{l,b} \eta(s^2 + \sum_{\alpha} t^{\dagger}_{lb\alpha}t_{lb\alpha} - 1) \tag{A7}$$

where $t^{(\dagger)}_{lb\alpha}$ labels triplets in unit cell l at basis site $b = A, B$ of the two interpenetrating triangular lattices comprising the hexagonal lattice. The sites $\widetilde{m}A$ in Eq. (A5) refer to the three nearest neighbors of the honeycomb basis around each of the triangular lattice sites at lB and the $\widetilde{l}$ labels the three nearest neighbors on each of the triangular lattices. $\widetilde{j_1} = j_1 - j_x$ and j_2 are the dimensionless exchange couplings. s^2 is the singlet condensate, and η the global Lagrange multiplier for constraint (A2).

This Hamiltonian can be diagonalized by standard Bogoliubov transformation leading to an energy E *per unit cell*, i.e. per two dimers, of

$$E = -\frac{3}{4} - \frac{3}{2}s^2 - 2\eta s^2 + 5\eta + \frac{3}{2N}\sum_{k}(E_{k+} + E_{k-}) \tag{A8}$$

with the *triplon dispersion*

$$E_{k\pm} = a\sqrt{1 \pm \frac{s^2}{a}e_{\pm}(k)} \tag{A9}$$

where

$$e_{\pm}(k) = \widetilde{j}_1\sqrt{3 + 2\cos(k_x) + 4\cos(\frac{k_x}{2})\cos(\frac{\sqrt{3}k_y}{2})}$$
$$\pm 2j_2(\cos(k_x) + 2\cos(\frac{k_x}{2})\cos(\frac{\sqrt{3}k_y}{2})) \tag{A10}$$
$$\equiv \widetilde{j}_1\sqrt{3 + g(k)} \pm j_2\, g(k) \tag{A11}$$

and $a = 1/4 - \eta$. Eqs. (A9)-(A11) display an important symmetry for $\widetilde{j}_1 \leftrightarrow -\widetilde{j}_1$, namely for that $e_{\pm}(k) \leftrightarrow -e_{\mp}(k)$. This implies, that on the quadratic level of the BO-HP and BO-MFT all results of the theory will be symmetric w.r.t. diagonal $j_1 = j_x$

From (A8)-(A11) the BO-HP is completed by replacing the sum of the first four addends in Eq. (A8) with to $-9/2$ and by setting $a = 1$, $s = 1$ in (A9, A10).

For the BO-MFT the energy E has to be extremized, implying two self-consistency equations $\partial_a E/\partial a = 0$ and $\partial_s E/\partial s = 0$. These can be combined into a single one for the parameter $d = s^2/a$, i.e.

$$d = \frac{5}{2} - \frac{3}{4N}\sum_{k,v=\pm} \frac{1}{\sqrt{1 + v\, d\, e_v(k)}}\,. \tag{A12}$$

Knowing d, both mean field parameters can be obtained from substituting into either one of the mean field equations, e.g. $\partial_a E/\partial a = 0$

$$2s^2 = 5 - \frac{3}{2N}\sum_{k,v=\pm}\frac{1+\frac{1}{2}\,v\,d\,e_v(k)}{\sqrt{1+v\,d\,e_v(k)}}\,. \tag{A13}$$

We mention in passing, that the trivial limit, i.e. $\widetilde{j}_1 = j_2 = 0$, leads to $d = 1$, $s = 1$, and $\eta = -3/4$, and therefore to a *singlet-triplet gap* of $\Delta = 1$ and a ground state energy of $E = -3/2$, which is consistent with two saturated singlets per unit cell.

Appendix B: Schwinger Boson Mean-Field Approach

In the Schwinger-boson representation, the Heisenberg interaction can be written as a bi-quadratic form. The spin operators are replaced by two species of bosons via the relation[48–50]

$$\vec{\mathbf{S}}_\alpha(\vec{r}) = \frac{1}{2}\vec{\mathbf{b}}^\dagger_\alpha(\vec{r})\cdot\vec{\sigma}\cdot\vec{\mathbf{b}}_\alpha(\vec{r}), \tag{B1}$$

where $\vec{\mathbf{b}}_\alpha(\vec{r})^\dagger = (\mathbf{b}^\dagger_{\alpha,\uparrow}(\vec{r}), \mathbf{b}^\dagger_{\alpha,\downarrow}(\vec{r}))$ is a bosonic spinor corresponding to the site α in the unit cell sitting at $\vec{r}$. $\vec{\sigma}$ is the vector of Pauli matrices, and there is a boson-number restriction $\sum_\sigma \mathbf{b}^\dagger_{\alpha,\sigma}(\vec{r})\mathbf{b}_{\alpha,\sigma}(\vec{r}) = 2S$ on each site.

In terms of boson operators we define the $SU(2)$ invariants

$$\mathbf{A}_{\alpha\beta}(\vec{x},\vec{y}) = \frac{1}{2}\sum_\sigma \sigma\mathbf{b}_{\alpha,\sigma}(\vec{x})\mathbf{b}_{\beta,-\sigma}(\vec{y}) \tag{B2}$$

$$\mathbf{B}_{\alpha\beta}(\vec{x},\vec{y}) = \frac{1}{2}\sum_\sigma \mathbf{b}^\dagger_{\alpha,\sigma}(\vec{x})\mathbf{b}_{\beta,-\sigma}(\vec{y}). \tag{B3}$$

The operator $\mathbf{A}_{\alpha\beta}(\vec{x},\vec{y})$ creates a spin singlet pair between sites α and β corresponding to unit cells located at $\vec{x}$ and $\vec{y}$ respectively. The operator $\mathbf{B}_{\alpha\beta}(\vec{x},\vec{y})$ creates a ferromagnetic bond, which implies the inter-site coherent hopping of the Schwinger bosons.

In this representation, the rotational invariant spin-spin interaction can be written as

$$\vec{\mathbf{S}}_\alpha(\vec{x})\cdot\vec{\mathbf{S}}_\beta(\vec{y}) =: \mathbf{B}^\dagger_{\alpha\beta}(\vec{x},\vec{y})\mathbf{B}_{\alpha\beta}(\vec{x},\vec{y}) : -\mathbf{A}^\dagger_{\alpha\beta}(\vec{x},\vec{y})\mathbf{A}_{\alpha\beta}(\vec{x},\vec{y})$$

where $:\mathbf{O}:$ denotes the normal ordering of the operator $\mathbf{O}$. One of the advantages of this rotational invariant decomposition is that it enables to treat ferromagnetism and antiferromagnetism on equal footing. This decomposition has been successfully used to describe quantum disordered phases in two-dimensional frustrated antiferromagnets[12,15,21,40,51–54].

In order to generate a mean field theory, we perform the Hartree-Fock decoupling

$$\begin{aligned}(\vec{\mathbf{S}}_\alpha(\vec{x})\cdot\vec{\mathbf{S}}_\beta(\vec{y}))_{MF} = [&B^*_{\alpha\beta}(\vec{x}-\vec{y})\mathbf{B}_{\alpha\beta}(\vec{x},\vec{y})\\ &- A^*_{\alpha\beta}(\vec{x}-\vec{y})\mathbf{A}_{\alpha\beta}(\vec{x},\vec{y})]\\ &- \langle(\vec{\mathbf{S}}_\alpha(\vec{x})\cdot\vec{\mathbf{S}}_\beta(\vec{y}))_{MF}\rangle\end{aligned} \tag{B4}$$

where the mean field parameters are given by

$$A^*_{\alpha\beta}(\vec{x}-\vec{y}) = \langle\mathbf{A}^\dagger_{\alpha\beta}(\vec{x},\vec{y})\rangle, \tag{B5}$$

$$B^*_{\alpha\beta}(\vec{x}-\vec{y}) = \langle\mathbf{B}^\dagger_{\alpha\beta}(\vec{x},\vec{y})\rangle, \tag{B6}$$

and the exchange at the mean field level is

$$\langle(\vec{\mathbf{S}}_\alpha(\vec{x})\cdot\vec{\mathbf{S}}_\beta(\vec{y}))_{MF}\rangle = |B_{\alpha\beta}(\vec{x}-\vec{y})|^2 - |A_{\alpha\beta}(\vec{x}-\vec{y})|^2. \tag{B7}$$

The mean field equations (B5) and (B6) must be solved in a self-consistent way together with the following constraint for the number of bosons in the system

$$B_{\alpha\alpha}(\vec{R}=\vec{0}) = 4N_c S, \tag{B8}$$

where N_c is the total number of unit cells and S is the spin strength. Self-consistent solutions in the bilayer honeycomb lattice involve finding the roots of coupled nonlinear equations for the mean field parameters and solving the constraints to determine the values of the Lagrange multipliers $\lambda^{(\alpha)}$ which fix the number of bosons in the system. We perform the calculations for large systems and extrapolate the results to the thermodynamic limit. Details of the self consistent calculation can be found in Refs. 12 and 21.

Appendix C: Series expansion

The D-SE calculations start from the limit of isolated dimers. To this end we decompose the Hamiltonian given by Eq.(1) in units of J_0 into

$$H = H_0 + V(j_1, j_x, j_2), \tag{C1}$$

where H_0 represents decoupled interlayer dimers and $V(j_1, j_x, j_2)$ is the interaction part of Hamiltonian, connecting dimers via j_1, j_x, j_2 couplings.

By construction the levels structure of H_0 is equidistant, which allows to sort the spectrum of H_0 in a block-diagonal form, where each block is labeled by an energy quantum-number Q. Therefore, Q=0 represents the ground state (*vacuum*), i.e., all dimers are in the singlet state. Q=1 sector is composed by states obtained by creating (from vacuum state) one-elementary triplet excitation (*particle*) on a given dimer, and so on. The cases in which $Q \geq 2$ will be of multi-particle nature.

In general the action of $V(j_1, j_x, j_2)$ mixes different Q-sectors, so that the block-diagonal form of H_0 is not conserved in H. However because of the ladder structure of the unperturbed spectrum, is possible to restore the block-diagonal form by application of continuous unitary transformations, using the flow equation method of Wegner[55]. This method can be implemented perturbatively order by order, transforming H onto an effective Hamiltonian H_{eff} which is block-diagonal in the quantum number Q, having the structure

$$H_{\text{eff}} = H_0 + \sum_{n,m,l}^{\infty} C_{n,m,l} j_1^n j_x^m j_2^l, \tag{C2}$$

where $C_{n,m,l}$ are weighted products of terms in $V(j_1, j_x, j_2)$ which conserve the Q-number, with weights determined by recursive differential equations, details of which can be found in Ref. 56.

Due to Q-number conservation several observables can be calculated directly from H_{eff} in terms of a D-SE in j_1, j_x, j_2. For systems with coupled spin-plaquettes continuous unitary transformations D-SE has been used for one[32], two[57–60] and three[61] dimensions. For the present model we have performed $O(4)$ D-SE in j_1, j_x, j_2 for ground state energy ($Q = 0$) and for $Q = 1$ sectors, respectively. We refer for technical details about the calculation to ref.[62]. Note finally that the contribution of perturbation in the case $V(j_1, j_1, 0)$ is *zero*, reflecting the invariance of original Hamiltonian under $j_1 \leftrightarrow j_x$ exchange.

Appendix D: Linear Spin Wave Theory at $j_1 = j_x$

Here we briefly quote the equations necessary to determine the critical coupling j_1^c for the first order IDP↔II quantum phase transition along the line $j_1 = j_x$ from linear spin wave theory. In the IDP along the latter line, the ground state energy is

$$E_{\text{all } L=0 \text{ sector}}/J_0 = -\frac{3}{2} N_\triangle \,, \tag{D1}$$

where $N_\triangle$ is the number of triangular unit cells. The Hamiltonian of the "all $L = 1$ sector" on the other hand reads

$$H_{\text{all } L=1 \text{ sector}}/J_0 = \frac{1}{2} N_\triangle + j_1 \sum_{\langle lm \rangle} \mathbf{L}_l \cdot \mathbf{L}_m \,, \tag{D2}$$

where the sum refers to an $S = 1$ Heisenberg antiferromagnet on the hexagonal lattice. The ground state of the latter is known to be an Néel state with an energy per *site* to $O(1/S)$ of[63]

$$\begin{aligned} E_{LSWT} &= j_1 \left\{ -\frac{3S^2}{2} + \frac{S}{4\pi^2\sqrt{2}} \int_0^{2\pi} \int_0^{2\pi} dx\, dy\, [3 - \right. \\ &\qquad \left. \cos(x) - \cos(y) - \cos(x+y)]^{1/2} - \frac{3S}{2} \right\} \\ &\simeq j_1 \left(-\frac{3S^2}{2} - 0.314763\, S \right) . \end{aligned} \tag{D3}$$

For $S = 1$ this yields the line

$$E_{LSWT} \simeq -1.81476\, j_1 \,, \tag{D4}$$

which is plotted in Fig. 5. Together with (D1, D2) and keeping in mind that a '*site*' in (D3) refers to *two* spins on the original bilayer, this implies that $1.81476\, j_1^c = 1$, i.e.

$$j_1^c \simeq 0.551036$$

* zhanghao@iphy.ac.cn
† lamas@fisica.unlp.edu.ar
‡ w.brenig@tu-bs.de

[1] P. W. Anderson, science **235**, 1196 (1987).
[2] G. Misguich and C. Lhuillier, in *Frustrated Spin Systems* (World Scientific, 2005).
[3] L. Balents, Nature **464**, 199 (2010).
[4] C. Lhuillier and G. Misguich, in *Introduction to Frustrated Magnetism* (Springer-Verlag, 2011).
[5] O. Smirnova, M. Azuma, N. Kumada, Y. Kusano, M. Matsuda, Y. Shimakawa, T. Takei, Y. Yonesaki, and N. Kinomura, J. Am. Chem. Soc. **131**, 8313 (2009).
[6] H. C. Kandpal and J. van den Brink, Phys. Rev. B **83**, 140412(R) (2011).
[7] M. Matsuda, M. Azuma, M. Tokunaga, Y. Shimakawa, and N. Kumada, Phys. Rev. Lett. **105**, 187201 (2010).
[8] A. Mulder, R. Ganesh, L. Capriotti, and A. Paramekanti, Phys. Rev. B **81**, 214419 (2010).
[9] F. Wang, Phys. Rev. B **82**, 024419 (2010).
[10] S. Okumura, H. Kawamura, T. Okubo, and Y. Motome, J. Phys. Soc. Jpn. **79**, 114705 (2010).
[11] B. Clark, D. Abanin, and S. Sondhi, Phys. Rev. Lett. **107**, 087204 (2011).
[12] D. C. Cabra, C. A. Lamas, and H. D. Rosales, Phys. Rev. B **83**, 094506 (Mar 2011).
[13] R. Ganesh, D. Sheng, Y.-J. Kim, and A. Paramekanti, Phys. Rev. B **83**, 144414 (2011).
[14] A. F. Albuquerque, D. Schwandt, B. Hetényi, S. Capponi, M. Mambrini, and A. M. Läuchli, Phys. Rev. B **84**, 024406 (2011).
[15] D. Cabra, C. Lamas, and H. Rosales, Mod. Phys. Lett. B **25**, 891 (2011).
[16] F. Mezzacapo and M. Boninsegni, Phys. Rev. B **85**, 060402(R) (2012).
[17] P. H. Y. Li, R. F. Bishop, D. J. J. Farnell, and C. E. Campbell, Phys. Rev. B **86**, 144404 (2012).
[18] R. F. Bishop, P. H. Y. Li., D. J. J. Farnell, and C. E. Campbell, J. Phys.: Condens. Matter **24**, 236002 (2012).
[19] R. Ganesh, J. van den Brink, and S. Nishimoto, Phys. Rev. Lett. **110**, 127203 (2013).
[20] Z. Zhu, D. A. Huse, and S. R. White, Phys. Rev. Lett. **110**, 127205 (2013).
[21] H. Zhang and C. Lamas, Phys. Rev. B **87**, 024415 (2013).
[22] S.-S. Gong, D. Sheng, O. I. Motrunich, and M. P. Fisher, Phys. Rev. B **88**, 165138 (2013).
[23] R. F. Bishop, P. H. Y. Li, D. J. J. Farnell, and C. E. Campbell, J. Phys.: Condens. Matter **25**, 306002 (2013).
[24] R. Ganesh, S. V. Isakov, and A. Paramekanti, Phys. Rev. B **84**, 214412 (2011).
[25] J. Oitmaa and R. Singh, Phys. Rev. B **85**, 014428 (2012).

[26] H. Zhang, M. Arlego, and C. A. Lamas, Phys. Rev. B **89**, 024403 (2014).
[27] I. Bose and S. Gayen, Phys. Rev. B **48**, 10653(R) (1993).
[28] I. Bose, Phys. Rev. B **45**, 13072 (1992).
[29] A. Honecker, F. Mila, and M. Troyer, Eur. Phys. J. B **15**, 227 (2000).
[30] W. Brenig and K. W. Becker, Phys. Rev. B **64**, 214413 (2001).
[31] W. Brenig, A. Honecker, and K. W. Becker, Advances in Solid State Physics, Springer Berlin Heidelberg, Editor: B. Kramer, **42**, 457 (2002).
[32] M. Arlego and W. Brenig, Eur. Phys. J. B **53**, 193 (2006).
[33] P. Chen, C.-Y. Lai, and M.-F. Yang, Phys. Rev. B **81**, 020409 (2010).
[34] O. Derzhko, T. Krokhmalskii, and J. Richter, Phys. Rev. B **82**, 214412 (2010).
[35] C. A. Lamas and J. M. Matera, Phys. Rev. B **92**, 115111 (2015).
[36] Preliminary results for $E[\Delta]_{MFT}(0<j_1<0.36, j_1'=0)$ by M. Arlego, C. A. Lamas, and Wolfram Brenig have been displayed in[37].
[37] M. Arlego, C. A. Lamas, and H. Zhang, J. Phys.: Conf. Ser. **568**, 042019 (2014).
[38] A. Mezio, C. N. Sposetti, L. O. Manuel, and A. E. Trumper, Europhysics Letters **94**, 47001 (1997).
[39] S. Sachdev and R. N. Bhatt, Phys. Rev. B **41**, 9323 (1990).
[40] A. Trumper, L. Manuel, C. Gazza, and H. Ceccatto, Phys. Rev. Lett. **78**, 2216 (1997).
[41] R. L. Doretto and M. Vojta, Phys. Rev. B **85**, 104416 (2012).
[42] V. N. Kotov, O. Sushkov, Z. Weihong, and J. Oitmaa, Phys. Rev. Lett. **80**, 5790 (1998).
[43] D. G. Joshi, K. Coester, K. P. Schmidt, and M. Vojta, Physical Review B **91**, 094404 (2015).
[44] D. G. Joshi and M. Vojta, Physical Review B **91**, 094405 (2015).
[45] A. V. Chubukov, JETP Lett. **49**, 129 (1989).
[46] A. V. Chubukov and T. Jolicoeur, Phys. Rev. B **44**, 12050(R) (1991).
[47] S. Sachdev and R. N. Bhatt, Phys. Rev. B **41**, 9323 (1990).
[48] A. Auerbach and D. P. Arovas, Phys. Rev. Lett. **61**, 617 (Aug 1988).
[49] A. Auerbach, *Interacting Electrons and Quantum Magnetism* (Springer-Verlag, New York, 1994).
[50] A. Auerbach and D. P. Arovas, in *Introduction to Frustrated Magnetism* (Springer, 2011).
[51] H. Ceccatto, C. Gazza, and A. Trumper, Phys. Rev. B **47**, 12329 (1993).
[52] A. Mezio, C. Sposetti, L. Manuel, and A. Trumper, Eur. Phys. Lett. **94**, 47001 (2011).
[53] L. Messio, B. Bernu, and C. Lhuillier, Phys. Rev. Lett. **108**, 207204 (2012).
[54] L. Messio, C. Lhuillier, and G. Misguich, Phys. Rev. B **87**, 125127 (2013).
[55] F. Wegner, Ann. Phys. **506**, 77 (1994).
[56] C. Knetter and G. S. Uhrig, Eur. Phys. J. B **13**, 209 (2000).
[57] W. Brenig and A. Honecker, Phys. Rev. B **65**, 140407(R) (2002).
[58] M. Grzeschik and W. Brenig, Phys. Rev. B **69**, 064420 (2004).
[59] M. Arlego and W. Brenig, Phys. Rev. B **75**, 024409 (2007).
[60] M. Arlego and W. Brenig, Phys. Rev. B **78**, 224415 (2008).
[61] W. Brenig, Phys. Rev. B **67**, 064402 (2003).
[62] M. Arlego and W. Brenig, Phys. Rev. B **84**, 134426 (2011).
[63] E. Rastelli, A. Tassi, and L. Reatto, Physica B+C **97** (1979).